



**HAL**  
open science

# Exchange of Water Between the Ross Gyre and ACC Assessed by Lagrangian Particle Tracking

Christopher J. Roach, Kevin Speer

► **To cite this version:**

Christopher J. Roach, Kevin Speer. Exchange of Water Between the Ross Gyre and ACC Assessed by Lagrangian Particle Tracking. *Journal of Geophysical Research. Oceans*, 2019, 124 (7), pp.4631-4643. 10.1029/2018JC014845 . hal-02520731

**HAL Id: hal-02520731**

**<https://hal.science/hal-02520731>**


Submitted on 31 Aug 2021

**HAL** is a multi-disciplinary open access archive for the deposit and dissemination of scientific research documents, whether they are published or not. The documents may come from teaching and research institutions in France or abroad, or from public or private research centers.

L'archive ouverte pluridisciplinaire **HAL**, est destinée au dépôt et à la diffusion de documents scientifiques de niveau recherche, publiés ou non, émanant des établissements d'enseignement et de recherche français ou étrangers, des laboratoires publics ou privés.

Copyright

## Exchange of Water Between the Ross Gyre and ACC Assessed by Lagrangian Particle Tracking

Christopher J. Roach<sup>1,2</sup>  and Kevin Speer<sup>3</sup>

<sup>1</sup>LOCEAN, Paris, France, <sup>2</sup>Institute for Marine and Antarctic Studies, University of Tasmania, Hobart, Tasmania, Australia, <sup>3</sup>Geophysical Fluid Dynamics Institute, and Earth, Ocean and Atmospheric Science, Florida State University, Tallahassee, FL, USA

### Key Points:

- Using numerical particle tracking we examine the location and vertical structure of inflow to the Ross Gyre
- We estimate that 2.6 Sv enters the gyre from the ACC and 2.9 Sv from the AA margins
- Most of the inflow from the ACC into the gyre is associated with low-frequency variability

### Supporting Information:

- Supporting Information S1

### Correspondence to:

C. J. Roach,  
christopher-john.roach@locean-ipsl.upmc.fr

### Citation:

Roach, C. J., & Speer, K. (2019). Exchange of water between the Ross Gyre and ACC assessed by Lagrangian particle tracking. *Journal of Geophysical Research: Oceans*, 124, 4631–4643. <https://doi.org/10.1029/2018JC014845>

Received 5 DEC 2018

Accepted 18 JUN 2019

Accepted article online 26 JUN 2019

Published online 8 JUL 2019

**Abstract** To reach upwelling and downwelling zones deep within the Southern Ocean seasonal sea ice cover, water masses must move across the Antarctic Circumpolar Current and through current systems including the Ross Gyre, Weddell Gyre, and Antarctic Slope Current. In this study we focus our attention on the Lagrangian exchange between the Ross Gyre and surrounding current systems. We conducted numerical experiments using five-day 3-D velocity fields from the Southern Ocean State Estimate with a particle tracking package to identify pathways by which waters move from near the Antarctic coastal margins or Antarctic Circumpolar Current into the interior of the Ross Gyre, and to identify the time scales of variability associated with these pathways. Waters from near the Antarctic margins enter the Ross Gyre along the western and northern boundaries of gyre until the gyre separates from the Pacific-Antarctic Ridge near fracture zones. At this juncture, Antarctic Circumpolar Current-derived inflow dominates the across-gyre transport up to the Antarctic margin. Transport and exchange associated with different time-average components of flow are calculated to determine the relative contributions of high- and low-frequency and time-mean components.

**Plain Language Summary** Formation of cold, dense waters in the Antarctic Zone south of the Polar Front plays a key role in driving the overturning circulation, with major implications on global climate. One of the key regions of dense water formation is the Ross Sea. However, between the Ross Sea and the wider Southern Ocean lies the Ross Gyre. So we need to understand how the Ross Gyre controls exchange between the continent and the Southern Ocean. We use velocities from a numerical model to track virtual water parcels as they move into the gyre. This lets us estimate total inflow and identify pathways the water takes to enter the gyre. We find that inflow into the Ross Gyre is enough to replace outflowing dense waters from the Ross Sea. We also find that most inflow enters via exchange with Antarctic Circumpolar Current at the northern and eastern limits of the gyre through a combination of eddy activity and low-frequency variability in the gyre boundary.

## 1. Introduction

Interactions in the Southern Ocean between waters of the Antarctic margin, the Antarctic Circumpolar Current (ACC), and intervening gyres with a strong seasonal sea ice cover play a major role in the climate system (Rintoul, 2018). In the Antarctic Zone, south of the Polar Front, upwelling along deep isopycnal surfaces and mixing brings deep waters to the surface, closing the upper cell of the Meridional Overturning Circulation (Marshall & Speer, 2012), while the formation of dense water on the Antarctic margin and associated entrainment plays a key role in the formation of Antarctic Bottom Water and Modified Circumpolar Deep Water, thereby driving the lower cell of the meridional overturning circulation (Lumpkin & Speer, 2007; Orsi et al., 2002).

However, to reach the upwelling zone and eventually the coastal margin from the interior of the Southern Ocean, or the opposite, water parcels must pass through systems of currents and gyres, including fronts of the ACC, the Weddell and Ross Gyres, and the Antarctic Slope Current (ASC). Depending upon local dynamics these currents and gyres can act to either suppress or enhance exchange between the wider Southern Ocean and the Antarctic margins, controlling, in turn, the properties of the water masses formed within the gyres and those spreading away from the continent (Couldrey et al., 2013; Fahrbach et al., 2011; Orsi & Wiederwohl, 2009).

We focus our attention on the Ross Gyre (Figure 1) and examine the question of the exchange between the gyre and the surrounding environment—which comprises the ACC to the north and the Antarctic margin, including the Antarctic Slope Current to the south. To some degree, the Ross Gyre acts as both a buffer and carrier of properties from one side to the other. The Ross Gyre has been identified as a major source of Circumpolar Deep Water inflow to the Amundsen and Bellingshausen Seas, with implications on heat transport and resulting melt of ice shelves (Nakayama et al., 2018), and as a receptacle of basal meltwater flowing off the Ross Sea shelf (Kusahara & Hasumi, 2014).

A measure of these effects is the exchange rate between the interior and exterior of the mean gyre, as water parcels entering the gyre tend to have long residence times there. Locations of enhanced exchange are expected to be found at the two zonal extremes—east and west—of the gyre since water masses from widely different regions are brought into contact there as the flow is oriented away from or toward the continent. Orsi and Wiederwohl (2009) have described the detailed evolution and transport of water masses from the slope region to the interior in the western Ross Gyre, adjacent to the Ross Sea. These modified waters enter the interior moving along the northern rim of the gyre. At the eastern limit of the gyre, deep water from farther north approaches the continent and upwells, exerting an influence on both sea ice and shelf water masses (Assmann & Timmermann, 2005).

Compared to the Weddell Gyre (Fahrbach et al., 2011), the Ross Gyre region (Gouretski, 1999) is not as well observed by Argo floats and ship-transects and, while the quality of satellite altimetry in regions of ice coverage has improved greatly in recent years (Armitage et al., 2018; Bulczak et al., 2015; Dotto et al., 2018), resolution is still limited to about 50 km and offers only a surface view of the geostrophic currents. Thus, our attention turns to numerical model output to obtain information about the vertical structure of flow. We make use of the Southern Ocean State Estimate (SOSE), which incorporates observations from altimetry and hydrography combined with the MIT GCM (general circulation model), to derive estimates of gyre-induced exchange rates.

We conducted a total of three Lagrangian particle release experiments. The first used five-day SOSE velocity fields to resolve entrainment due to eddy activity and other high-frequency processes. The second experiment used 90-day low-pass-filtered fields to suppress the contribution of eddy activity and thereby isolate entrainment associated with low-frequency variability of the gyre boundary. The final experiment used time-mean fields to determine exchange associated with the time-mean velocity field.

We describe SOSE in section 2. Our choice of gyre boundary and the particle tracking methodology are described in section 3. Results are presented in section 4, and we discuss the implication of our results and potential limitations arising from the data set and approach in section 5.

## 2. The Southern Ocean State Estimate of Ross Gyre Circulation

We obtained the velocity fields from the Southern Ocean State Estimate version 2 (Iter 100, June 2014 release, <http://sose.ucsd.edu>). Based on the MIT GCM numerical model, SOSE (Mazloff et al., 2010) assimilates both in situ, satellite and reanalysis data including Argo float, ship-board, and XBT temperature and salinity profiles; atmospheric forcing from National Centers for Environmental Prediction–National Center for Atmospheric Research (2005–2007) and ERA-Interim (2008–2010); satellite-derived sea surface temperatures; and merged Topex/Poseidon-Jason-1 sea level anomalies. SOSE covers the time period between January 2005 and December 2010 at  $1/6^\circ$  horizontal resolution over a total of 42 depth levels unevenly distributed between the surface and 5,575 m; all fields are available as one- and five-day averages. In this study we use the five-day averaged fields.

Surface waves are capable of transporting water and other properties near the surface, but are not resolved by SOSE. Fraser et al. (2018) recently described the surface wave-driven Stokes drift in velocity fields showing that this effect makes it much easier for water-parcels close to the surface to cross the ACC. These and similar effects are neglected here.

Extensive prior validation work has been done on SOSE, demonstrating good agreement with air-sea fluxes from other products (Cerovečki et al., 2011; Cerovečki & Mazloff, 2015); water mass mean properties (Cerovečki & Mazloff, 2015), near-surface hydrography, and sea ice (Abernathey et al., 2016); and vertical structure in the Drake Passage region (Firing et al., 2011). Our own comparisons in the

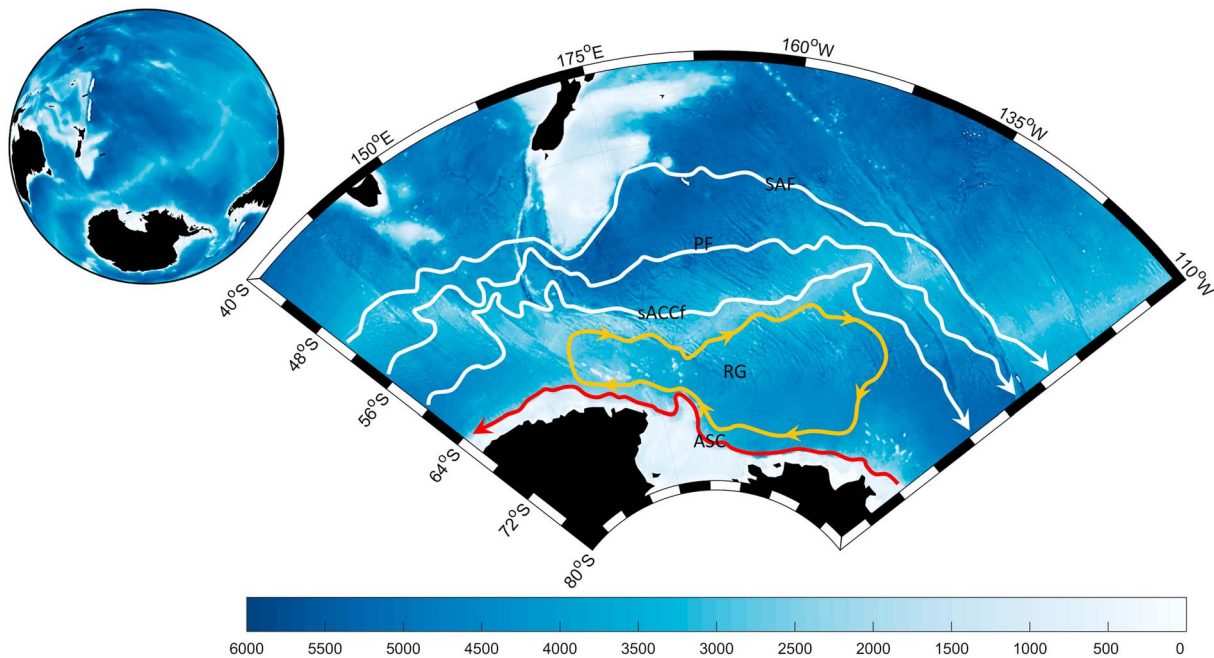


**Figure 1.** The Ross Gyre (RG; indicated in orange) and surrounding flow regime including the major fronts of the Antarctic Circumpolar Current (white) including the Sub-Antarctic Front (SAF), Polar front (PF) and Southern ACC front (sACCF); and Antarctic Slope Current (ASC; red), superimposed on ETOPO (Amante, 2009) bathymetry, in meters, as shown by the white-blue range in the color bar.

region 130°E–110°W of temperature and salinity sections and Argo trajectory-derived velocities (see supporting information) demonstrated reasonable agreement with SOSE data.

### 3. Method

#### 3.1. Defining the Gyre

In order to determine the exchange of water between the interior and exterior of the gyre, it was necessary to define the gyre boundary. We opted to define the gyre boundary in terms of the depth-integrated (here barotropic) streamfunction obtained by integrating the zonal velocity field northward from the coast and from the seafloor to the surface.

Considering previous studies (Dellnitz et al., 2009; Dotto et al., 2018) which identify significant variability in gyre structure we considered using a time-varying boundary. However, while we found significant variability (white contours in Figure 2 show a subset of time-varying  $-8$ -Sv contours) we did not find a clear separation of gyre structure into a monthly or semiannual component with our definition of depth-integrated transport. As a result, we opted to define a time-mean gyre boundary and distinguish fluctuating components of exchange according to higher and lower frequencies as described below.

The Ross Gyre streamfunction strength estimated here is close to 20 Sv consistent with prior estimates of recirculation from SOSE (Mazloff et al., 2010). The gyre boundary was defined by choosing a streamfunction contour lying farther outside and enclosing the central gyre. It was necessary to balance maximizing the recirculating flow captured by our gyre definition with other considerations, for instance some definitions, such as the  $-4$ -Sv contour, produced boundaries which included narrow extensions wrapped closely around the continental margin. While similar coastal extensions of the gyre have been seen in prior model (Rickard et al., 2010) and satellite altimetry studies (Dotto et al., 2018) we maintain a stricter definition of the gyre boundary, ultimately settling on  $-8$  Sv as the outermost time-mean closed contour that did not display coastal extensions (Figure 2).

#### 3.2. Lagrangian Particle Tracking in the Ross Gyre

We used the Connectivity Modelling System v2.0 (Paris et al., 2013) to advect particles through 3-D, time-evolving velocity fields from the Southern Ocean State Estimate. Particles were released at five-day

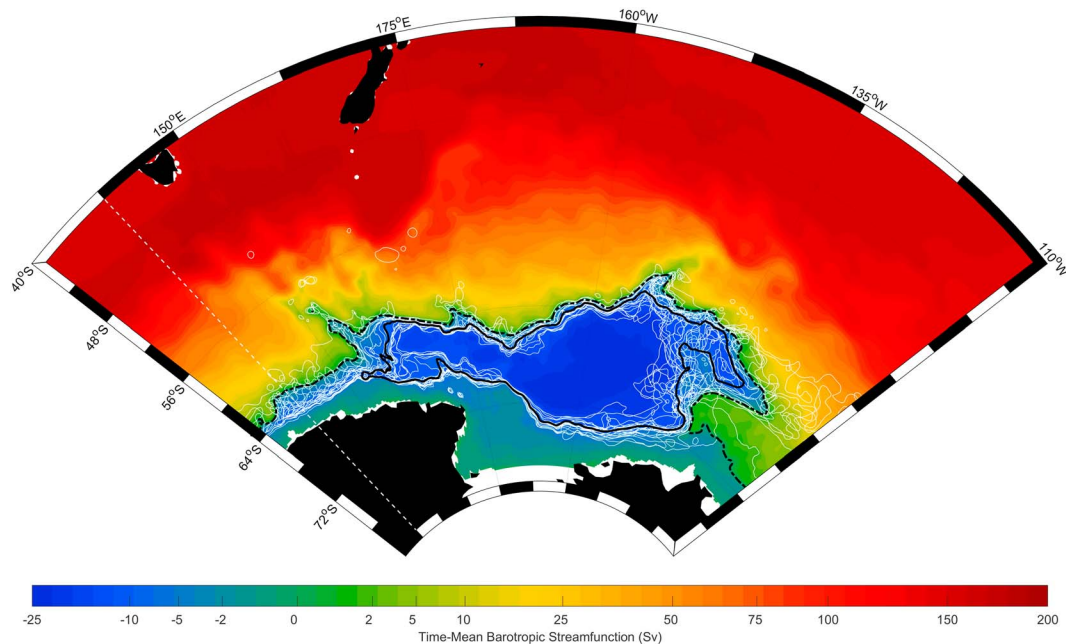


**Figure 2.** SOSE time-mean barotropic streamfunction (Sv). Superimposed are the time-mean (solid black) and time-varying (solid white) gyre boundaries defined by the  $-8$ -Sv barotropic contour streamfunction, along with the release line (dashed white) and the time-mean 0-Sv contour (dashed black) used to define the boundary between ACC and AA margin particles on the release line. Note that the color scale is nonlinear.

intervals along a release line between the Antarctic Coast and Australia at  $140^{\circ}\text{E}$ ; this choice of release intervals was decided by considering the temporal resolution of SOSE and the choice of release times used in previous studies (Van Sebille et al., 2012; Van Sebille et al., 2014). Particles were spaced at  $0.25^{\circ}$  intervals along the release lines, with vertical separation of 100 m in the upper 2,000 m, and 200 m between 2,000 m and the seafloor. In order to estimate transport we followed a methodology previously applied to the Agulhas leakage (Van Sebille et al., 2010) and Tasman Leakage (Van Sebille et al., 2012; Van Sebille et al., 2014), whereby we label each particle with a transport estimated as the surface area of a cell surrounding each particle's release location ( $\Delta y \cdot \Delta z$ ) multiplied by the velocity normal to the release line.

To obtain a stable estimate of transport we continue looping over the six years of SOSE data to give a total of 24 years of particle releases, with a total of  $4.9 \times 10^6$  particles released per experiment. Each individual particle was tracked until it grounded, left the domain, or exceeded an age of 10 years. A given particle was classified as having become entrained in the gyre if it met three criteria:

1. The particle had crossed the contour defining the boundary of the time-mean gyre (our choice of contours is discussed above).
2. The particle had spent a minimum of 100 days within the time-mean gyre.
3. The particle also passed through a box bounded by  $170^{\circ}\text{E}$ ,  $140^{\circ}\text{W}$ , and  $67^{\circ}\text{S}$  and the Antarctic coast.

The last two criteria were selected as we wish to identify and isolate inflow into the gyre which leads to sustained entrainment of waters instead of inflow of water parcels which briefly enter the gyre before rapidly escaping back into the Southern Ocean. This analysis is meant to identify Lagrangian pathways into the gyre, not to examine the overall mass balance of the gyre, which is satisfied locally by the model. Thus, as described below, we find contributions to the inflow to the gyre from different regions and quantify these contributions according to their transport. Of course, outflow occurs as well, mainly in surface and bottom layers, but the details of the outflow are not the focus of this study.

We conducted three experiments, the first using the five-day mean SOSE velocity fields, the second 90-day mean fields, and the third using time mean fields. This allows us to separate the transport associated with high-frequency (e.g., eddies) and low-frequency (e.g., seasonal variability) variability from the time-mean flow. Velocity fields for the 90-day experiment were produced by smoothing the five-day fields using a



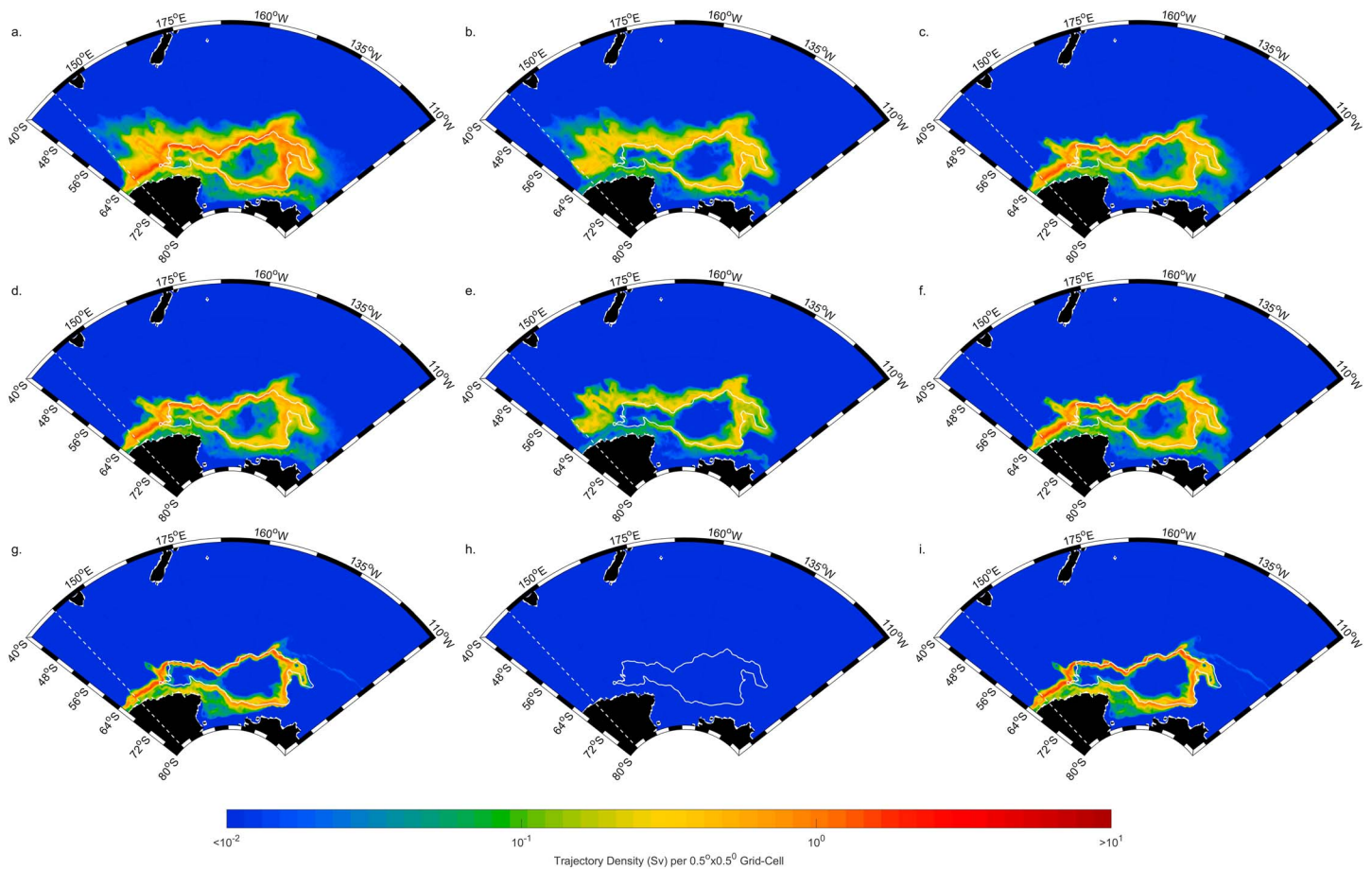


**Figure 3.** Trajectory density map (in Sv; note the logarithmic color scale) of particles released at  $140^{\circ}\text{E}$  and subsequently entrained into the gyre. (a–c) The 5-day experiment, (d–f) the 90-day experiment, and (g–i) the time-mean experiment. The left column (a, d, and g) shows the transport pathways for all entrained particles, with the middle column (b, e, and h) showing particles originating in the ACC and the right column (c, f, and i) particles originating near the coast. The solid white line indicates the time-mean gyre boundary and the dashed white line indicates the 0-Sv contour used to define the near shelf regime at the release line.

90-day wide boxcar filter, while fields for the time-mean experiment were created by computing a temporal average over all time steps of the five-day fields.

To examine the sources of inflow into the gyre we label each particle as originating either within the Antarctic (AA) margins (here taken as all release locations between the coast and 0-Sv time-mean stream function contour; see the dotted black line in Figure 2) or in the “broader” Southern Ocean and ACC (all particles released north of the 0-Sv contour).

#### 4. Results

Maps showing transport pathways between the release lines and the gyre are shown in Figure 3. These maps were computed in a manner similar to Van Sebille et al. (2012): for each particle that entered the gyre we converted its trajectory into a binary map on a  $0.5^{\circ} \times 0.5^{\circ}$  grid showing which cells the particle passed through, each binary map was then multiplied by the particle's tagged transport, and finally the transport-weighted maps for particular subset of particles were summed up and normalized by the total number of release-days to produce each map of transport pathways.

Examining the full transport fields (Figure 3, left column) we find that transport is strongly intensified in proximity to the gyre boundaries and coast with weaker transport to the north and within the gyre interior. The region of strong exchange remains robust in all experiments; however, the outer bands of the region of weaker transport recede toward the gyre boundary as we increase the smoothing of the velocity fields.

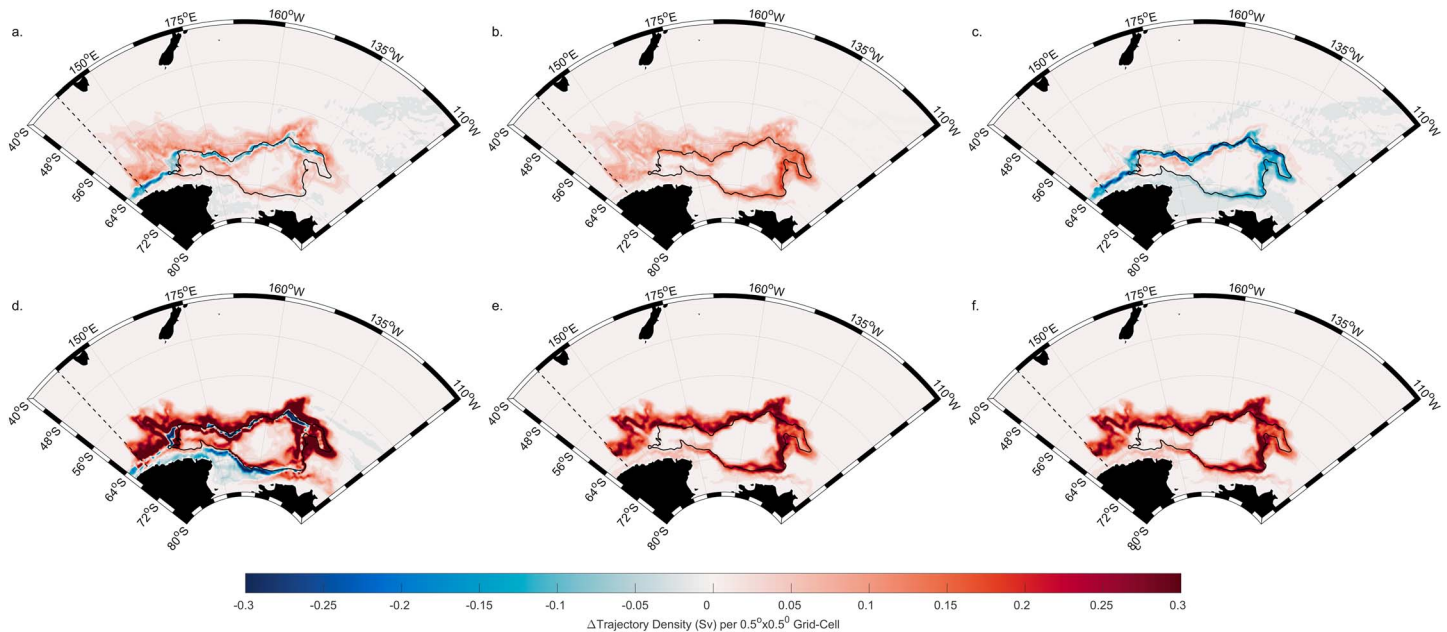


**Figure 4.** Differences between trajectory density maps (Sv) for different levels of smoothing and particle origins. (a–c) The difference between 5- and 90-day mean SOSE fields and (d–f) the difference between 90-day and time-mean SOSE fields. The columns show, from left to right, all transport (a and d), transport originating in the ACC (b and e), and transport originating near the coast (c and f). Positive values correspond to dominance by the less smoothed of the two fields. The solid black line indicates the time-mean gyre boundary and the dashed black line indicates the release line.

This is particularly clear in proximity to the release line. As we increase the smoothing we see the area of weak exchange move south, from about 50°S in the five-day fields to 60°S in the 90-day fields up to the ASC for time-mean fields. This behavior is consistent with the suppression of higher-frequency variability (e.g., eddies) and subsequently lower frequency variability (e.g., seasonal variations) as we increase the smoothing.

Decomposing the exchange by the particle source (Figure 3, middle and right columns) we find that transport from the Southern Ocean-ACC into the gyre is split between the eddy-scale and seasonal variability, with little contribution from the time-mean flow. Transport from the AA margins into the gyre, on the other hand, is dominated by low-frequency variability and time-mean flow.

To better quantify this partitioning between eddy scales and seasonal variability we produced maps of the difference between 5- and 90-day mean transport (Figure 4). Examining the total transport difference (left column) we see that lower frequency variability is dominant over higher frequencies along the northern boundary of the gyre, while eddy activity apparently dominates within the gyre interior and to the north of the gyre. Transport from particles released within the ACC is dominated by high-frequency variability. Transport from the AA margins is dominated by low-frequency variability near the western and eastern limits of the gyre boundary, but, like the all-transport case, higher-frequency variability is significant both in the gyre interior and to the north of the gyre. Similar results of the difference between 90-day and time-mean fields (Figure 4, bottom) show that the mean flow is dominant over low-frequency variability near the gyre boundary for both the all-transport and AA margin cases, with low-frequency variability dominant away from the gyre boundary.

Time series of inflow transport into the gyre (not shown) indicates an initial ramp-up period of about 2,000 days, subsequently inflow plateaus to a mean value of 5.7 Sv. Of this, 2.6 Sv originates in the ACC with the remaining 3.1 Sv originating near the AA margins. Applying a 90-day low-pass filter to the velocity fields reduces total inflow to 5.10 Sv, with inflow from the ACC reducing by one third to 1.68 Sv while inflow from near the AA margins increases to 3.42 Sv. Meanwhile, the time-mean inflow is 2.86 Sv, 2.84 Sv from sources within the AA margins with no significant (0.02 Sv) contribution from the ACC. Examination of the time-mean streamfunction indicates that most of the transport from the AA margins is associated with a

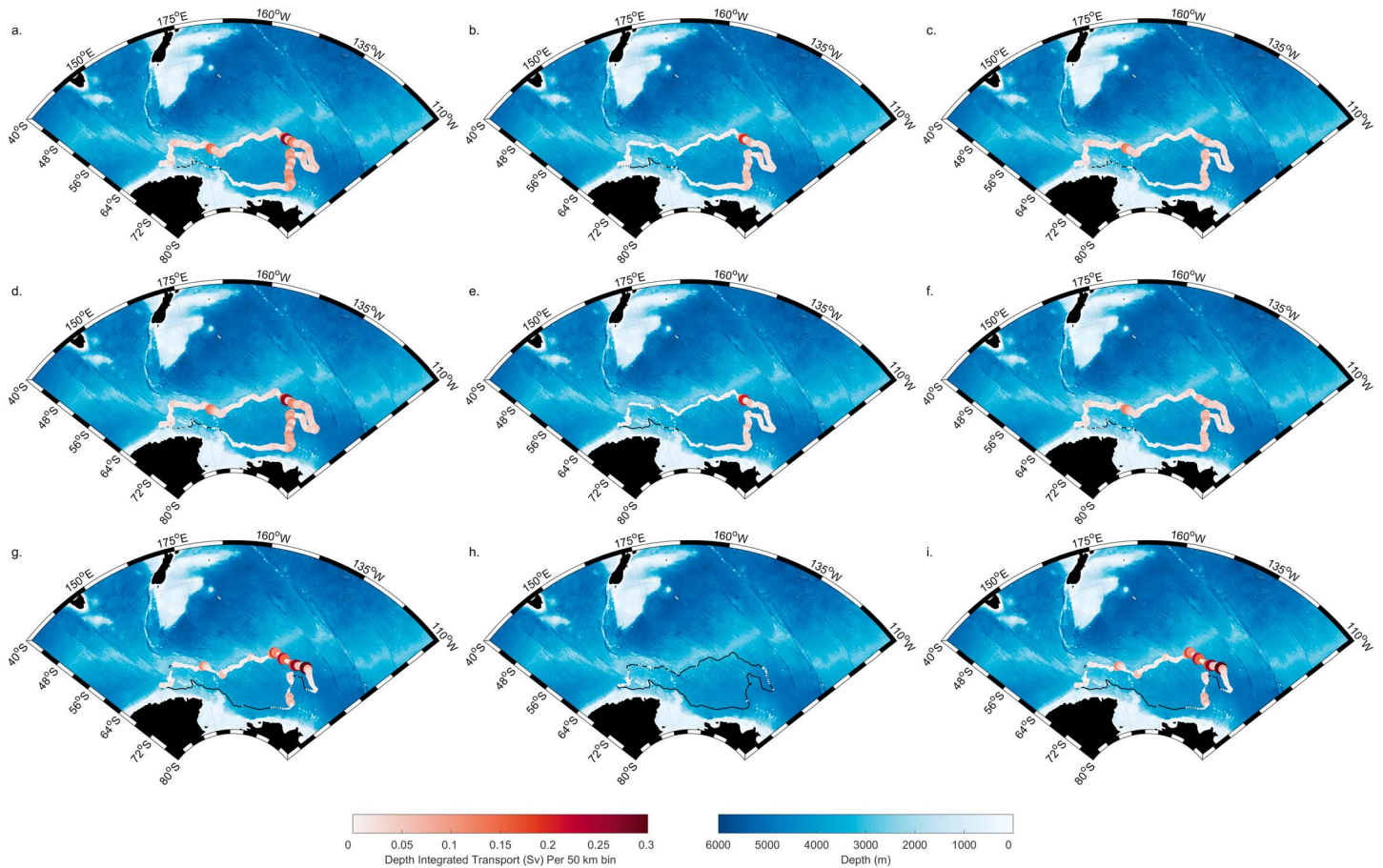


**Figure 5.** Vertically integrated mean transport into the gyre (Sv; indicated by both color and size) partitioned into 50-km along-gyre boundary bins superimposed on maps of bottom topography. (a–c) The 5-day experiment, (d–f) the 90-day experiment, and (g–i) the time-mean experiment. The left column (a, d, and g) shows the transport pathways for all entrained particles, with the middle column (b, e, and h) showing particles originating in the ACC and the right column (c, f, and i) particles originating near the coast. The solid black line indicates the time-mean gyre boundary. Note that while the color scale is the same in all panels, sizes are not.

narrow “trough” of streamfunction, centered about 64°N, connected to the outer fringes of the gyre, with little inflow originating between the coast and the southern flank of this gyre extension.

These results indicate that ACC waters enter the gyre either within eddies or through seasonal variability in gyre structure such as fluctuations of the gyre boundary and changes in mixed layer depth. AA margin waters instead predominantly enter the gyre by following time-mean flow paths associated with a coastal extension of the gyre, with a secondary contribution of about 0.6 Sv from low-frequency variability. The association of time-mean AA margin sourced transport with the coastal extension of the gyre suggests that we may be resolving recirculation of gyre waters or coastal waters entrained further east (Kusahara & Hasumi, 2014) rather than an inflow of coastal waters originating near the release line.

We further examined the locations at which particles entered the gyre (Figure 5). The gyre can broadly be broken into three regions: a western region ending at a “bend” in the Pacific-Antarctic Ridge (PAR) near 180°E, a central region between the bend in the PAR to the point where the gyre diverges from the PAR near 150°W, and the eastern region between the gyre diverging from the PAR and the coast. In general, the western region is characterized by a moderate level of inflow, the central region displays very little inflow, and strong inflow is observed in the eastern region.

We note particularly strong inflow in proximity to the PAR bend near 180°E and immediately after the gyre-PAR divergence near 150°W. The strong inflow seen near 150°W in both 5- and 90-day smoothed fields is broadly consistent with the region where Gouretski (1999) identified an inflow of Upper CDW (UCDW)



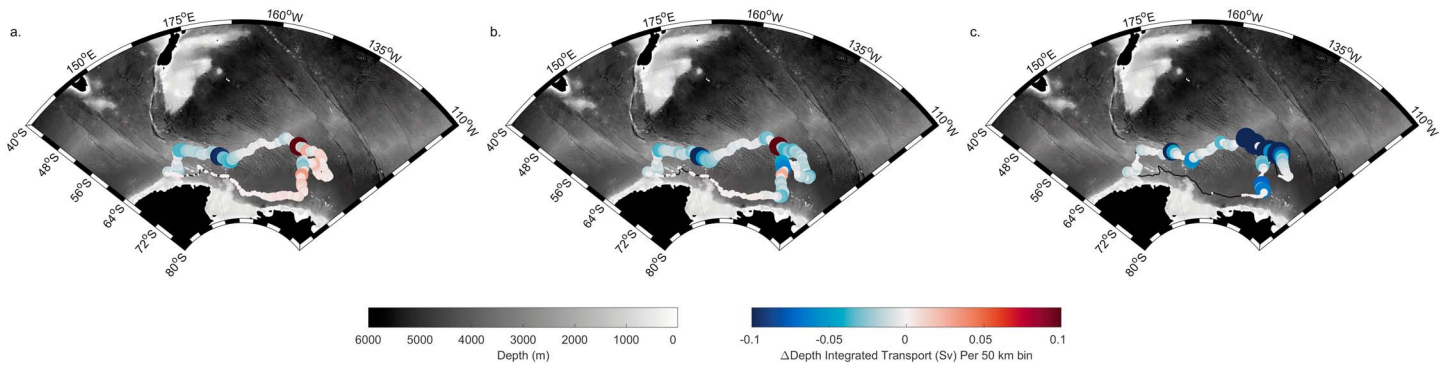


**Figure 6.** Differences in transport into the gyre (Sv) per 50 km along-gyre-boundary bins between ACC and AA margin inflow for (a) 5-day, (b) 90-day, and (c) time-mean SOSE fields. The solid black line indicates the time-mean gyre boundary and the dashed black line indicates the release line. Positive (red) values indicate areas where ACC sources contributed more than AA margin sources.

into the Ross Gyre. In the time-mean experiment we find inflow from the ACC is insignificant and inflow from the near the coast is heavily dominated by the region immediately after the gyre-PAR divergence, with smaller contributions near the bend in the PAR and the Antarctic coast.

In the five-day experiment inflow into the western region of the gyre is predominantly derived from the AA margins (Figure 6, left), with inflow to the eastern region approximately evenly partitioned between the AA margins and ACC sources (compare Figure 6, left and middle panels). In the smoothed (90-day) experiment inflow along virtually the entire gyre boundary is dominated by AA margin-derived transport (Figure 6, right). Examining the difference between 5- and 90-day experiment inflows we find that in the case of ACC-derived waters (Figure 7, left) the 5-day inflow (resolving eddies; low-frequency variability and time-

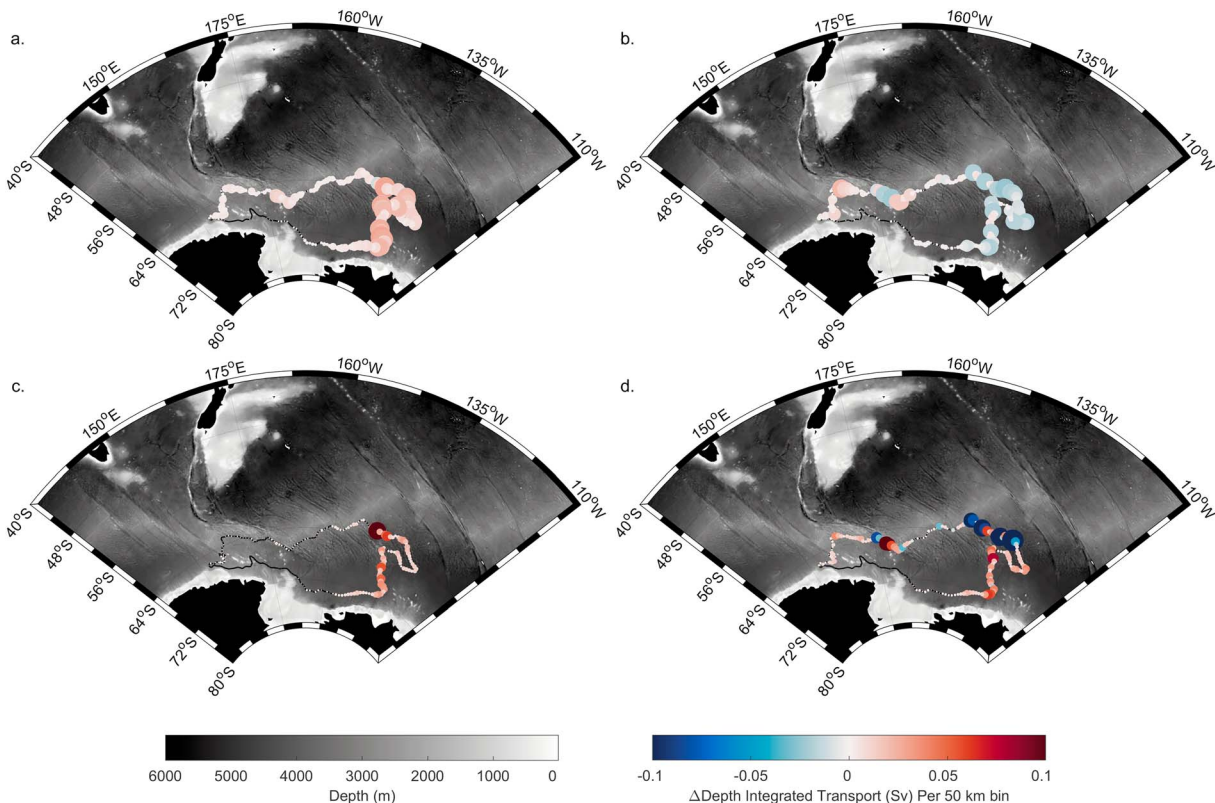


**Figure 7.** Differences in transport into the gyre (Sv) per 50 km along-gyre-boundary bins between different levels of smoothing ((a and b) 5- minus 90-day fields and (c and d) 90-day minus time-mean at bottom) for particles released in the ACC (a and c) and near the coast (c and d).

mean flow) is typically stronger than the 90-day inflow (resolving low-frequency variability and time-mean flow), which is in turn stronger than the time-mean inflow. This implies that eddies and low-frequency variability are the main drivers of this exchange. In the case of AA margin waters (Figure 7, right) we see that the 90-day experiment generally produced larger inflows than both the 5-day and time-mean experiments, suggesting that most of the inflow from AA margin sources is associated with lower frequency variability and time-mean inflows, with the exception of a region in the western limit of the gyre where eddy-mixing appears to be significant.

The structure of the inflow seen in the 5- and 90-day experiments is broadly comparable to the structure of inflow into the Weddell Gyre where previous studies (Ryan et al., 2016; Schröder & Fahrbach, 1999) indicate that exchange is mostly through eddy-driven mixing in the northeast boundary of the gyre, with lower frequency advective inflow along the eastern boundary.

A major component of this analysis is the information about the depths (Figures 8) and neutral densities at which particles cross the gyre boundary. Considering the 5- and 90-day SOSE fields we find that inflow can be split into the same three regimes described above:

1. Along the gyre's northwestern boundary (0 to 3,000 km, approximately 180°E) we see both surface-intensified (<1,500-m depth) inflow and lower intensity inflow in the ocean interior. The surface-intensified inflow is predominantly sourced from the ASC, while the ocean-interior inflow is partitioned approximately evenly between ACC and AA margin sources.
2. Towards the center and north-east of the gyre boundary (3,000–5,000 km), inflow at first diminishes before increasing between 4,000 and 5,000 km along the gyre boundary (coinciding with the divergence of the gyre from the PAR). Over most of this range inflow extends to about 2,000-m depth and is roughly evenly partitioned between ACC and AA margin-derived water parcels.
3. Along the gyre's eastern boundary (5,000–8,000 km after separation from the PAR) the depth to which inflow reaches steadily diminishes from about 2,000 to less than 500 m.

The time-mean fields, as discussed above, show that virtually all inflow comes from the ASC and is concentrated in a small number of strongly surface-intensified jets, extending to about 1,000-m depth.

Examining a map (Figure 9) of potential vorticity (PV; here estimated as  $\frac{f}{\rho} \frac{d\rho}{dz}$ ), estimated from SOSE density fields at 243-m depth we find that the area of highest inflow (NE of the gyre) is collocated with a region of homogenized PV. We see other regions of more moderate inflow (e.g., the eastern and western flanks of the gyre) where the gyre boundary crosses PV contours, while we see little inflow in regions where the gyre boundary follows PV contours.

Examining the neutral densities at which transport occurs (Figure 10), using definitions of water masses given in Abernathy et al. (2016), we find that in all cases the vast majority (85–87%) of inflow to the gyre occurs within the Circumpolar Deep Water (CDW; 27.5–28.2 kg/m<sup>3</sup>). In the 5- and 90-day experiments the Lower CDW (28–28.2 kg/m<sup>3</sup>) contributes 46–49% of total inflow, with 36–40% occurring in the UCDW (27.5–28 kg/m<sup>3</sup>). Considering only waters originating in the ACC we find that about 50% enters the gyre as lower CDW and 34–36% enters as UCDW. The time-mean experiment is an exception in that UCDW accounts for 54% of the inflow, while lower CDW accounts for only 33% of the inflow, as noted above inflow from the ACC is minimal.

## 5. Discussion

We examined the origins of water that enters and remains in the Ross Gyre for a full season or more, and investigate how the sources of this inflow are split between waters originating near the coast and in the ACC. The total inflow from the AA margins and ACC into the gyre is 5.7 Sv with 55% of inflowing waters originating in the AA margins west of the gyre and the remaining 45% originating within the ACC. The flow pathway from the AA margins to the gyre interior is mostly associated with a coastal extension of the gyre, possibly indicative of recirculation of gyre waters or coastal waters entrained further east (Kusahara & Hasumi, 2014). Most inflow enters through the northeast corner, near the separation of the gyre boundary from the Pacific-Antarctic Ridge, and along the eastern boundary of the gyre. The separation of the gyre from the PAR allows a wider range of seasonal variability in the gyre boundary (Dotto et al., 2018) and likely

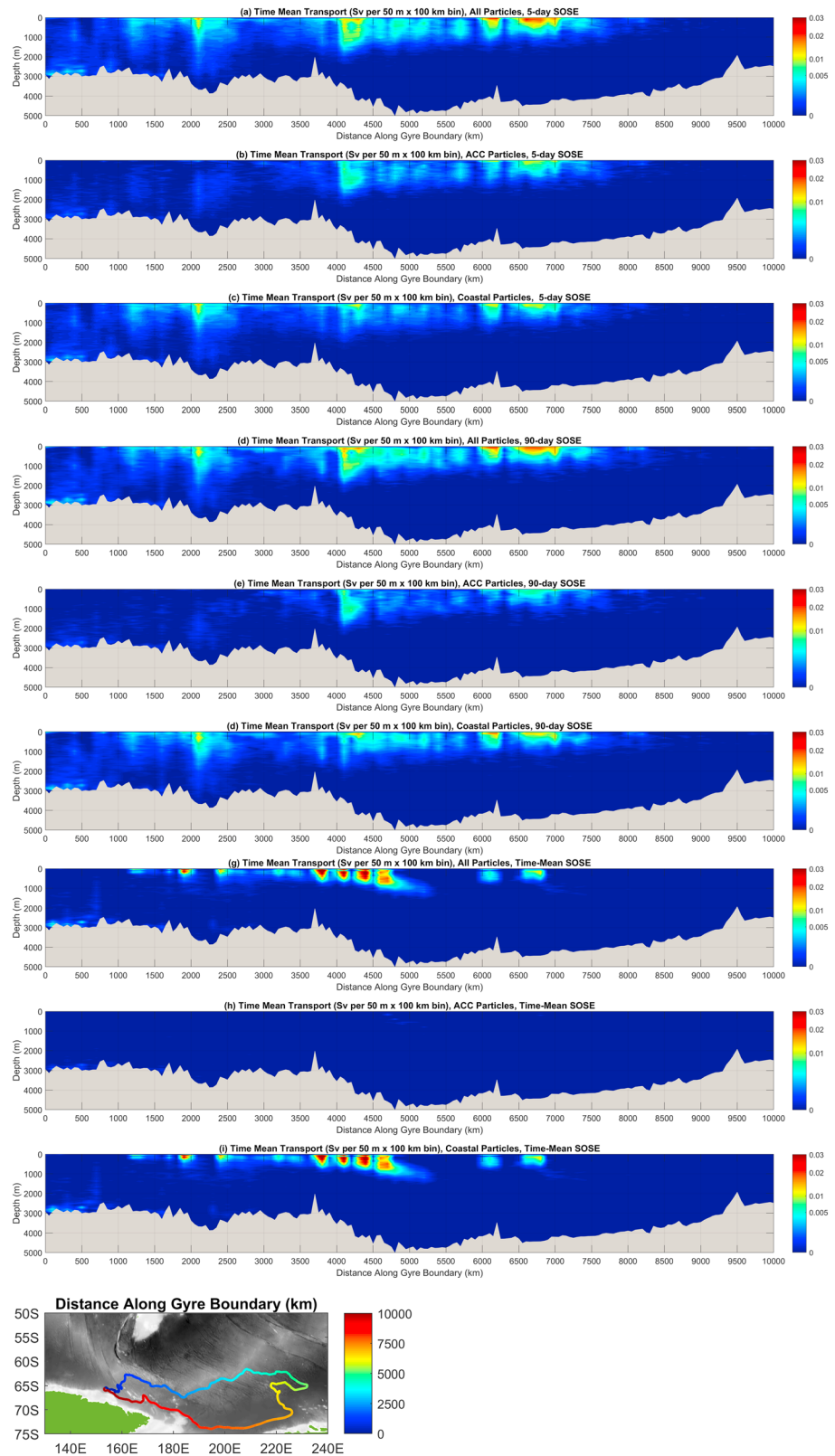


**Figure 8.** Distribution of time-mean transport into the gyre (Sv per  $100 \text{ km} \times 50 \text{ m}$  bin) as a function of depth and the distance along the time-mean gyre boundary, for (a–c) 5-day, (d–f) 90-day, and (g–i) time-mean experiments. Total transport (a, d, and g) is decomposed into ACC (b, e, and h) and AA margin (c, f, and i) sources. Distance is measured clockwise from the western limit of the gyre, as shown in the insert (bottom). Note that color scales are nonlinear.

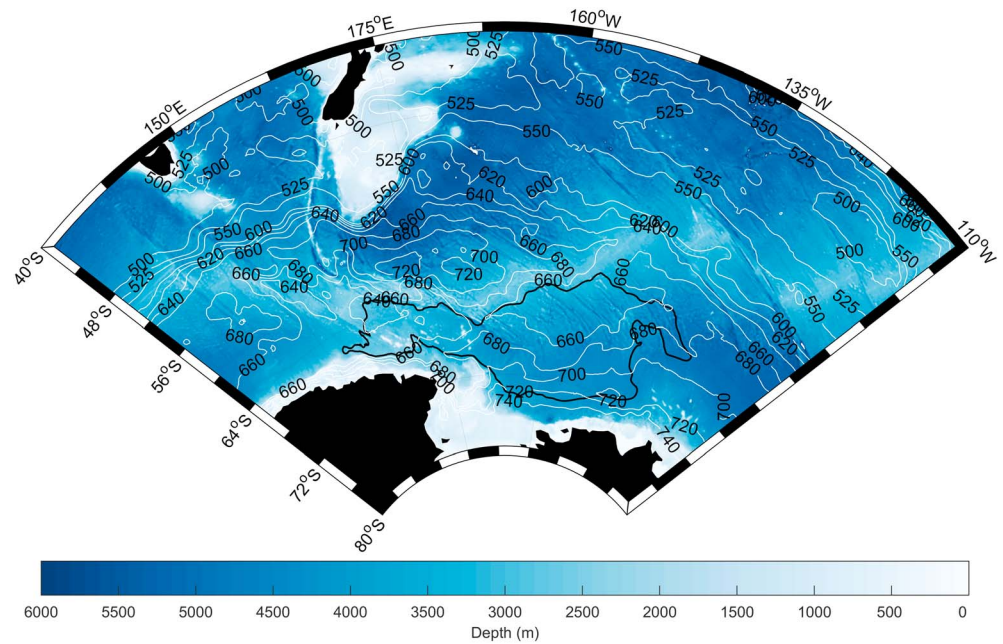


**Figure 9.** Time-mean potential vorticity ( $\times 10^{-12}$  m/s) at 243 m (white labeled contours) superimposed on bathymetry and the time-mean gyre boundary (black line).

enhances generation of eddies (Bracco & Pedlosky, 2003; Thompson & Sallée, 2012). There is also significant inflow in the far-western region of the gyre. We infer little inflow between 180°E and 150°W, where the PAR acts as a barrier to both eddy-derived inflow and low-frequency displacement of the front associated with the gyre boundary. Previous studies, while not quantifying inflow, have identified hydrographic features indicative of waters entering both the Ross Gyre (Gouretski, 1999) and Weddell Gyre (Ryan et al., 2016;

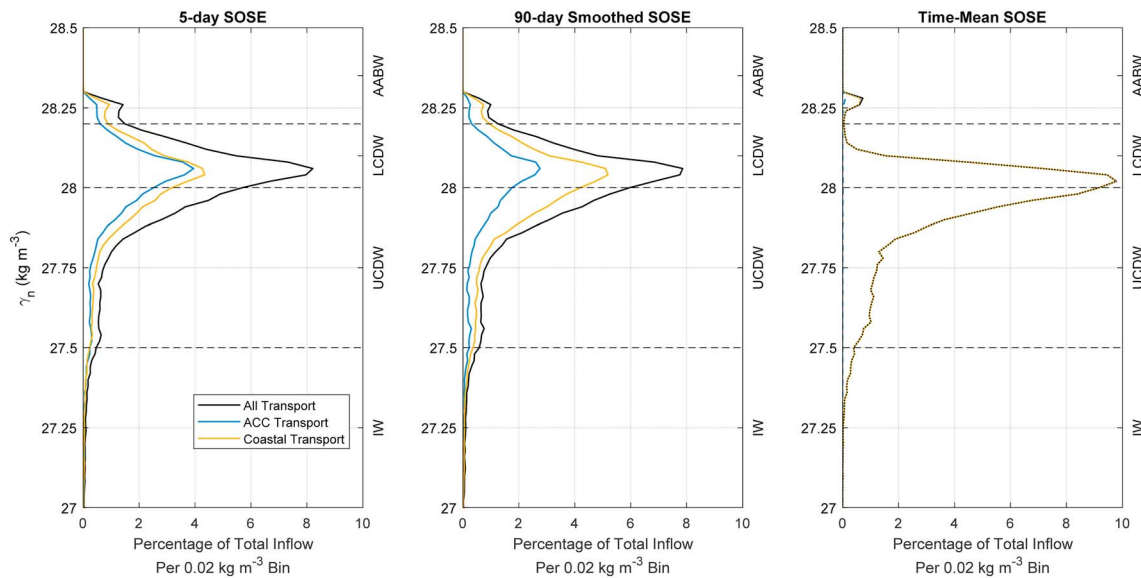


**Figure 10.** Percentage of total inflow to the gyre per  $0.02 \text{ kg m}^{-3}$  neutral density anomaly ( $\gamma_n$ ) bin for (left) 5-day, (middle) 90-day, and (right) time-mean SOSE velocity fields. Black lines indicate total transport (both ACC and AA margin sources) while blue lines indicate ACC sourced transport and the orange lines AA margin sourced transport. Note that ACC and AA margin transports are normalized by the total transport (including both sources) into the gyre for that experiment. Densities anomalies corresponding to the Intermediate Water (IW), Upper Circumpolar Deep Water (UCDW), Lower Circumpolar Deep Water (LCDW), and Antarctic Bottom Water (AABW) are shown on the with water mass boundaries indicated by the horizontal dashed black lines.



Schröder & Fahrbach, 1999) through the northeast margins of the gyres, similar to our inferences from SOSE. Seasonal-scale variability in the gyre suggests important Lagrangian exchange, and waters originating near the coast are found to enter the eastern regions of the gyre by a combination of seasonal-scale variability of the gyre and time-mean inflow, and to enter the western region predominantly due to eddies and low-frequency flow. We find that about two thirds of the inflow from the ACC is associated with seasonal-scale variability, likely meandering fronts, with the remaining one third from higher-frequency eddy fluctuations, and with almost all inflow from the ACC entering the gyre through the eastern boundary.

In terms of its vertical distribution, inflow to the western region of the gyre is found to occur throughout the water column. Moving east along the boundary the inflow increasingly becomes confined to the upper 2,000 m, before receding further to the upper 500 m as the eastern boundary of the gyre approaches the Antarctic coast.

In the eastern limit of the gyre ACC-sourced water masses predominantly enter the gyre in neutral density ranges associated with Lower and Upper Circumpolar Deep Waters. This suggests the Ross Gyre to be one of the receptacles of water in the Upper Cell. Parcels that skirt the gyre boundary but do not enter the gyre proceed west along the margin. Here they interact with the Antarctic margin and shelf in the Bellingshausen Sea and eastern Amundsen Seas, and, depending on their density, may reach the surface Ekman layer.

The inflow to the gyre is more than adequate to accommodate some of the 1.7–2.0 Sv of dense water exported from the Ross Sea shelf (Gordon et al., 2009; Whitworth & Orsi, 2006), along with other sources advected along the coast from Amundsen and Bellingshausen Seas (Nakayama et al., 2014). The dense water masses leaving the shelves are thought to exit the region westward along the slope for the most part; however, some of this water spreads into the interior at intermediate depths, and the broader vertical distribution of inflow in the western region, with indications of stronger inflow near the bottom, carries waters modified by convection on the shelf into the gyre.

#### Acknowledgments

In this study we made use of the YoMaHa'07 Argo float velocity data set (<http://apdrc.soest.hawaii.edu/projects/yomaha/>) and the Southern Ocean State Estimate ([http://sose.ucsd.edu/sose\\_stateestimation\\_data\\_05to10.html](http://sose.ucsd.edu/sose_stateestimation_data_05to10.html)). Both data sets are fully or partially derived from data made freely available through the International Argo Program and the national programs that contribute to it (<http://www.argo.ucsd.edu>, <http://argo.jcommops.org>). The Argo Program is part of the Global Ocean Observing System (<http://doi.org/10.17882/42182>).

#### References

- Abernathy, R. P., Ceroveck, I., Holland, P. R., Newsom, E., Mazloff, M., & Talley, L. D. (2016). Water-mass transformation by sea ice in the upper branch of the Southern Ocean overturning. *Nature Geoscience*, 9(8), 596–601. <https://doi.org/10.1038/ngeo2749>, <https://www.nature.com/articles/ngeo2749#supplementary-information>
- Amante, C. (2009). *ETOPO1 1 arc-minute global relief model: Procedures, data sources and analysis*. Boulder, Colo.: U.S. Dept. of Commerce, National Oceanic and Atmospheric Administration, National Environmental Satellite, Data, and Information Service, National Geophysical Data Center, Marine Geology and Geophysics Division.
- Armitage, T. W. K., Kwok, R., Thompson, A. F., & Cunningham, G. (2018). Dynamic topography and sea level anomalies of the Southern Ocean: Variability and teleconnections. *Journal of Geophysical Research: Oceans*, 123(1), 613–630. <https://doi.org/10.1002/2017JC013534>
- Assmann, K. M., & Timmermann, R. (2005). Variability of dense water formation in the Ross Sea. *Ocean Dynamics*, 55(2), 68–87. <https://doi.org/10.1007/s10236-004-0106-7>
- Bracco, A., & Pedlosky, J. (2003). Vortex generation by topography in locally unstable baroclinic flows. *Journal of Physical Oceanography*, 33(1), 207–219. [https://doi.org/10.1175/1520-0485\(2003\)033<0207:VGBTIL>2.0.CO;2](https://doi.org/10.1175/1520-0485(2003)033<0207:VGBTIL>2.0.CO;2)
- Bulczak, A. I., Bacon, S., Naveira Garabato, A. C., Ridout, A., Sonnewald, M. J. P., & Laxon, S. W. (2015). Seasonal variability of sea surface height in the coastal waters and deep basins of the Nordic Seas. *Geophysical Research Letters*, 42, 113–120. <https://doi.org/10.1002/2014GL061796>
- Ceroveck, I., & Mazloff, M. R. (2015). The spatiotemporal structure of diabatic processes governing the evolution of Subantarctic Mode Water in the Southern Ocean. *Journal of Physical Oceanography*, 46(2), 683–710. <https://doi.org/10.1175/JPO-D-14-0243.1>
- Ceroveck, I., Talley, L. D., & Mazloff, M. R. (2011). A comparison of southern ocean air–sea buoyancy flux from an ocean state estimate with five other products. *Journal of Climate*, 24(24), 6283–6306. <https://doi.org/10.1175/2011JCLI3858.1>
- Couldrey, M. P., Jullion, L., Naveira Garabato, A. C., Rye, C., Herráiz-Borreguero, L., Brown, P. J., et al. (2013). Remotely induced warming of Antarctic Bottom Water in the eastern Weddell gyre. *Geophysical Research Letters*, 40, 2755–2760. <https://doi.org/10.1002/grl.50526>
- Dellnitz, M., Froyland, G., Horenkamp, C., Padberg-Gehle, K., & Sen Gupta, A. (2009). Seasonal variability of the subpolar gyres in the Southern Ocean: A numerical investigation based on transfer operators. *Nonlinear Processes in Geophysics*, 16(6), 655–663. <https://doi.org/10.5194/npg-16-655-2009>
- Dotto, T., Garabato, A., Bacon, S., Tsamados, D. M., Holland, P. R., Hooley, J., et al. (2018). Variability of the Ross Gyre, Southern Ocean: Drivers and responses revealed by satellite altimetry. *Geophysical Research Letters*, 45, 6195–6204. <https://doi.org/10.1029/2018GL078607>
- Fahrbach, E., Hoppema, M., Rohardt, G., Boebel, O., Klatt, O., & Wisotzki, A. (2011). Warming of deep and abyssal water masses along the Greenwich meridian on decadal time scales: The Weddell gyre as a heat buffer. *Deep Sea Research Part II: Topical Studies in Oceanography*, 58(25–26), 2509–2523. <https://doi.org/10.1016/j.dsr2.2011.06.007>
- Firing, Y. L., Chereskin, T. K., & Mazloff, M. R. (2011). Vertical structure and transport of the Antarctic Circumpolar Current in Drake Passage from direct velocity observations. *Journal of Geophysical Research*, 116, C08015. <https://doi.org/10.1029/2011JC006999>
- Fraser, C. I., Morrison, A. K., Hogg, A. M., Macaya, E. C., van Sebille, E., Ryan, P. G., et al. (2018). Antarctica's ecological isolation will be broken by storm-driven dispersal and warming. *Nature Climate Change*, 8(8), 704–708. <https://doi.org/10.1038/s41558-018-0209-7>

- Gordon, A. L., Orsi, A. H., Muench, R., Huber, B. A., Zambianchi, E., & Visbeck, M. (2009). Western Ross Sea continental slope gravity currents. *Deep Sea Research Part II: Topical Studies in Oceanography*, *56*(13-14), 796–817. <https://doi.org/10.1016/j.dsr2.2008.10.037>
- Gouretski, V. (1999). The large-scale thermohaline structure of the Ross Gyre. In *Oceanography of the Ross Sea Antarctica*, (pp. 77–100). Milan: Springer.
- Kusahara, K., & Hasumi, H. (2014). Pathways of basal meltwater from Antarctic ice shelves: A model study. *Journal of Geophysical Research: Oceans*, *119*, 5690–5704. <https://doi.org/10.1002/2014JC009915>
- Lumpkin, R., & Speer, K. (2007). Global ocean meridional overturning. *Journal of Physical Oceanography*, *37*(10), 2550–2562. <https://doi.org/10.1175/JPO3130.1>
- Marshall, J., & Speer, K. (2012). Closure of the meridional overturning circulation through Southern Ocean upwelling. *Nature Geoscience*, *5*(3), 171–180. <https://doi.org/10.1038/ngeo1391>
- Mazloff, M. R., Heimbach, P., & Wunsch, C. (2010). An eddy-permitting Southern Ocean state estimate. *Journal of Physical Oceanography*, *40*(5), 880–899. <https://doi.org/10.1175/2009JPO4236.1>
- Nakayama, Y., Menemenlis, D., Zhang, H., Schodlok, M., & Rignot, E. (2018). Origin of Circumpolar Deep Water intruding onto the Amundsen and Bellingshausen Sea continental shelves. *Nature Communications*, *9*(1), 3403. <https://doi.org/10.1038/s41467-018-05813-1>
- Nakayama, Y., Timmermann, R., Rodehacke, C. B., Schröder, M., & Hellmer, H. H. (2014). Modeling the spreading of glacial meltwater from the Amundsen and Bellingshausen Seas. *Geophysical Research Letters*, *41*, 7942–7949. <https://doi.org/10.1002/2014GL061600>
- Orsi, A. H., Smethie, W. M., & Bullister, J. L. (2002). On the total input of Antarctic waters to the deep ocean: A preliminary estimate from chlorofluorocarbon measurements. *Journal of Geophysical Research*, *107*(C8), 3132. <https://doi.org/10.1029/2001JC000976>
- Orsi, A. H., & Wiederwohl, C. L. (2009). A recount of Ross Sea waters. *Deep Sea Research Part II: Topical Studies in Oceanography*, *56*(13-14), 778–795. <https://doi.org/10.1016/j.dsr2.2008.10.033>
- Paris, C. B., Helgers, J., van Sebille, E., & Srinivasan, A. (2013). Connectivity Modeling System: A probabilistic modeling tool for the multi-scale tracking of biotic and abiotic variability in the ocean. *Environmental Modelling & Software*, *42*(0), 47–54. <https://doi.org/10.1016/j.envsoft.2012.12.006>
- Rickard, G. J., Roberts, M. J., Williams, M. J., Dunn, A., & Smith, M. H. (2010). Mean circulation and hydrography in the Ross Sea sector, Southern Ocean: Representation in numerical models. *Antarctic Science*, *22*(5), 533–558. <https://doi.org/10.1017/S0954102010000246>
- Rintoul, S. R. (2018). The global influence of localized dynamics in the Southern Ocean. *Nature*, *558*(7709), 209–218. <https://doi.org/10.1038/s41586-018-0182-3>
- Ryan, S., Schröder, M., Huhn, O., & Timmermann, R. (2016). On the warm inflow at the eastern boundary of the Weddell Gyre. *Deep Sea Research Part I: Oceanographic Research Papers*, *107*, 70–81. <https://doi.org/10.1016/j.dsr.2015.11.002>
- Schröder, M., & Fahrbach, E. (1999). On the structure and the transport of the eastern Weddell Gyre. *Deep Sea Research Part II: Topical Studies in Oceanography*, *46*(1-2), 501–527. [https://doi.org/10.1016/S0967-0645\(98\)00112-X](https://doi.org/10.1016/S0967-0645(98)00112-X)
- Thompson, A. F., & Sallée, J.-B. (2012). Jets and topography: Jet transitions and the impact on transport in the Antarctic Circumpolar Current. *Journal of Physical Oceanography*, *42*(6), 956–972. <https://doi.org/10.1175/jpo-d-11-0135.1>
- Van Sebille, E., England Matthew, H., Zika Jan, D., & Sloyan Bernadette, M. (2012). Tasman leakage in a fine-resolution ocean model. *Geophysical Research Letters*, *39*, L06601. <https://doi.org/10.1029/2012GL051004>
- Van Sebille, E., Sprintall, J., Schwarzkopf, F. U., Gupta, A. S., Santoso, A., England, M. H., et al. (2014). Pacific-to-Indian Ocean connectivity: Tasman leakage, Indonesian Throughflow, and the role of ENSO. *Journal of Geophysical Research: Oceans*, *119*, 1365–1382. <https://doi.org/10.1002/2013JC009525>
- Van Sebille, E., Van Leeuwen, P. J., Biastoch, A., & de Ruijter, W. P. M. (2010). Flux comparison of Eulerian and Lagrangian estimates of Agulhas leakage: A case study using a numerical model. *Deep Sea Research Part I: Oceanographic Research Papers*, *57*(3), 319–327. <https://doi.org/10.1016/j.dsr.2009.12.006>
- Whitworth, T., & Orsi, A. H. (2006). Antarctic Bottom Water production and export by tides in the Ross Sea. *Geophysical Research Letters*, *33*, L12609. <https://doi.org/10.1029/2006GL026357>